

Self-induced corrosion of Ni-rich cathode materials by fluor-lithium salts

Hao Huang^{a,1}, Jingang Zheng^{a,1}, Hongyang Li^a, Siqi Guan^a, Hongwei Zhao^a, Weichen Han^a, Han Zhang^a, Guangshen Jiang^a, Lixiang Li^a, Baigang An^{a,*}, Chengguo Sun^{a,b,*}

^a School of Chemical Engineering University of Science and Technology Liaoning Anshan 114051, PR China

^b School of Chemical Engineering Nanjing University of Science and Technology, Nanjing 210094, PR China

ARTICLE INFO

Keywords:

Fluor-lithium salts
Ni-rich cathodic corrosion
Nickel ions induced
Voltage driving
Solid-state lithium metal battery

ABSTRACT

Fluor-lithium salts have been found for the serious aluminum collector corrosion in lithium-ion batteries. Herein, we unexpectedly observe that adding 10 wt% fluor-lithium salts into Ni-rich cathode can lead to irreversible decay of the initial discharge capacity. The capacity loss is related to the surface phase corrosion of Ni-rich cathode materials, where the local nickel ions work as catalytic sites to induce the breakage of the C-F bond in fluor-lithium salts, promoting the decomposition of fluor-lithium salts under the driving force of external voltage exceeding 1.93 V. The formation of F⁻ anion will attack Ni-rich cathode surface to produce nickel fluoride, resulting in the layered to rock-salt phase transformation. No corrosion behavior was found for iron, cobalt, and manganese of cathode materials. The synergistic activation by both nickel ions and voltage causes fluor-lithium salts to corrode the Ni-rich cathode materials.

1. Introduction

Development of solid-state lithium-ion batteries becomes the well-expectation to solve the low energy density and high flammability of liquid lithium batteries [1–3]. However, the solid-state electrolyte instead of organic liquid electrolyte has caused the poor point-to-point contact between cathode materials and electrolyte components [4–6], especially inside active cathode materials, without liquid electrolyte infiltration, it will result in slow Li-ions transport between cathode particles, and Li-ions deficient region during the cells charge/discharge process [7–11]. Therefore, when preparing the cathode electrodes with a high active material mass loading, apart from the conductive additive and binder, some solid-state electrolyte components or lithium salts are often added to improve the ion transport properties and electrochemical kinetics in the cathode materials [3,12–20]. In other case, pre-lithiation has been frequently adopted as an efficient strategy for compensating the initial Li-ions loss from the cathode upon the cathode-electrolyte interphase (CEI) formation.

As for lithium salts, several fluor-lithium salts including lithium bis(trifluoromethanesulfonyl)imide (LiTFSI), lithium difluoro(oxalato)borate (LiDFOB), and lithium bis(fluorosulfonyl)imide (LiFSI) are considered as the best candidates due to their high ionic conductivity and high thermal stability [21]. For example, a certain amount of liquid

electrolyte (3–10 μL) containing 1 mol L⁻¹ LiPF₆ was applied to wet the Ni-rich cathode (NCM622, NCM83) surface [12,13]. This treatment not only makes up for the shortage of lithium in cathode, but also can achieve good interfacial contact between electrode and solid electrolyte. The only drawback is that the liquid electrolyte will cause the dissolution of solid-state polymer electrolyte membrane, particularly for poly(ethylene oxide) (PEO)-based polymer electrolyte. In contrast, adding a small amount of polymer electrolytes or plastic crystal blended lithium salts into the cathode materials is widely adopted. Arrese-Igor et al. used about 15 wt% poly(propylene carbonate)-LiPSTFSI as a high-voltage tolerance of electrolyte for NCM622 electrode [15], Lee et al. reported the succinonitrile complexed with LiTFSI to form high ionic conductivity of additive in NCM83 cathode [3,16]. Because the identical components in both electrode and electrolyte membrane, it is beneficial to improve the affinity of the solid-solid interface contact, as well as mitigate the issues of insufficient transport of Li-ions in the cathode. In addition, given the fast ion transport properties of lithium salts or Li-ions conductors, about 10 wt% LiTFSI [17] or fast ionic conductor (Li₈ZrO₆) [18] was added in the cathode slurry as pre-lithiation additives for the irreversibly loss on the electrode surface due to the formation of CEI in the first cycle, especially for the charging process, no extra Li source is incorporated into the cathode to compensate for the first cycle Li-ions loss, it will result in a Li-ions deficient region inside the cathode, and

* Corresponding authors.

E-mail addresses: bgan@ustl.edu.cn (B. An), sunyangguo2004@163.com (C. Sun).

¹ These authors contributed equally to this work.

low first cycle coulombic efficiency. These studies all provide important insights into the effect of fluor-lithium salt additives on the transport, capacity and cycling performance of Li-batteries, yet it may be rare to correlate observations to corrosion behavior of surface phase in Ni-rich cathode materials. During a solid-state polymer Li-batteries test, we accidentally discovered that the addition of 10 wt% LiTFSI to the NCM622 cathode resulted in a significant reduction of 14 mAh g^{-1} in first discharge specific capacity in comparison to the cells without LiTFSI. To figure out the reasons of the decreased discharge capacity, we consulted the extensive research literatures, and there are two major reasons for this phenomenon. On the one hand, LiTFSI has the high highest occupied molecular orbitals (HOMO), thus easy to loss e^- , which tends to decompose into fluorine groups, such as F^- , CF_3^- , $SO_2CF_3^-$, etc., and participate in the formation of the solid interfacial layer [22–24]. Meanwhile, the aluminium current collector will be corroded in nonaqueous LiTFSI electrolytes under high voltage, which also may lead to irreversible capacity loss [25–26]. On the other hand, Ni-rich NCM cathodes easily suffer from severe parasitic side reactions during the lithiation/de-lithiation processes due to high oxidation capability of the Ni^{4+}/Ni^{3+} ions redox couple [27–33]. After long-term cycling of 100 cycles, NiF_2 and carbonate species can be found at the electrode surface, which can lead to irreversible dissolution of nickel from NCM622 cathode, and significant capacity fading [16,34]. However, we deduced that the above-mentioned reasons cannot be well account for our experimental phenomenon from the point of SEI formation and NCM622 degradation. Because the obvious reduction in initial discharge capacity was observed in our experiments, and the sample without LiTFSI displayed the normal discharge capacity, indicating the decreased discharge capacity of NCM622 is closely associated with the LiTFSI.

To figure out the effect of organic fluor-lithium salts on the capacity fading of Ni-rich cathode materials, herein, we investigated the capacity fading of the cathode initial discharge capacity by changing the addition of different types and contents of fluor-lithium salts to the cathode

material in a PEO-based solid electrolyte system. The contrast experiments reveal that the capacity loss is irrelevant to aluminium current collector corrosion, which is closely related to the serious surface phase corrosion of Ni-rich cathode materials. Combining theoretical calculations, X-ray photoelectron spectroscopy (XPS), transmission electron microscope (TEM), and in situ X-ray diffraction (XRD) characterization techniques, we demonstrated that when application of external voltage exceeds 1.93 V, the Ni^{2+} ions of NCM cathode materials can act as metal catalytic sites to induce the breakage of C-F bond in organic fluor-lithium salts, and promote the decomposition of organic fluor-lithium salts. The production of F group is able to combine Ni^{2+} ions of NCM cathode surface to generate NiF_2 , which leads to the corrosion behavior on the surface of NCM cathode, thus causing the capacity decay.

2. Results and discussion

To reduce the capacity fading caused by the solid-state polymer electrolyte [15,35], we prepared a typical composite electrolyte framework (PEO-LiClO₄-10 wt% LLZTO-10 wt% SN) to improve the interface compatibility and ionic conductivity [36–37]. All assembled cells were charged and discharged at 60 °C to eliminate the Li-ions transport imbalance. Fig. 1a shows the initial discharge capacity of NCM622 cathode with different additive contents of LiTFSI (10 wt%, 20 wt%, and 30 wt%). At 0.1 C rate with the voltage of 2.8–4.3 V, the Li||NCM622 cells deliver the first specific discharge capacity of 167.6, 140.3, 110.6 mAh g^{-1} for 10 wt%, 20 wt%, and 30 wt%, respectively. In contrast to the cells without LiTFSI that the capacity can reach 181.6 mAh g^{-1} , the results show that the initial performance degradation of cells become serious as increased the content of LiTFSI. Under the same conditions, other fluor-lithium salts additives (10 wt% LiFSI and 10 wt% LiDFOB) were used to replace the 10 wt% LiTFSI, the first discharge capacity of the NCM622 cathodes are much reduced about 20.1 mAh g^{-1} for LiFSI and 29.1 mAh g^{-1} for LiDFOB (Fig. 1b). Considering the initial

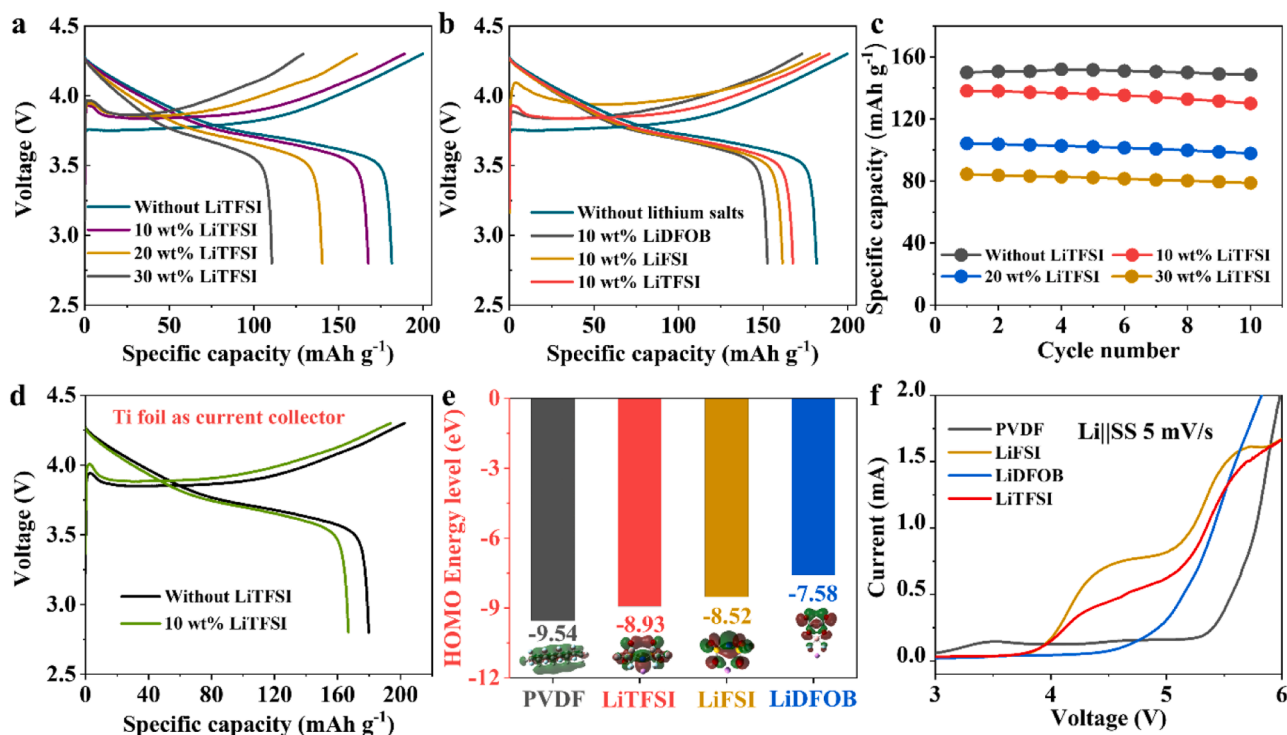


Fig. 1. (a) Discharge and charge voltage profiles of Li||NCM622 cells with different mass fractions of LiTFSI at 0.1 C and 60 °C. (b) Discharge and charge voltage profiles of Li||NCM622 cells with different fluor-lithium salts at 0.1 C and 60 °C. (c) Rate performance of Li||NCM622 cells with different mass fractions of LiTFSI at 0.1 C and 60 °C. (d) Discharge and charge voltage profiles of Li||NCM622 cells with/without LiTFSI at 0.1 C and 60 °C, the Ti foil as current collector. (e) Molecular orbital energy of different fluor-lithium salts and PVDF were calculated by density functional theory. (f) Oxidation stability of different Li-salts and PVDF were measured by linear sweep voltammetry.

capacity decay caused by the SEI formation, the cells with NCM622 cathode containing 0–30 wt% LiTFSI continue cycling to >10 cycles at 0.5 C, and the discharge capacity keep the steady trend without rebound phenomenon (Figs. 1c and S1). The results demonstrate that the fluor-lithium salts in cathode material can lead to an irreversible reduction in capacity and retention. Given the corrosion phenomenon occurred in the aluminum current collector with liquid electrolytes may lead to capacity decay, we used corrosion-resistant Ti foil instead of Al foil current collector to support the NCM622 cathode materials. As expected, the cell still delivered the decreased specific capacity about 13.8 mAh g⁻¹ in the first discharge (Fig. 1d) compared to the cell without LiTFSI. The scanning electron microscopy (SEM) images and XPS reveal that no corrosion happened on the surfaces of both Al and Ti foils after three cycles (Figs. S2a–c and S3a and b). In addition, we also used liquid 1 mol L⁻¹ LiTFSI-EC/DEC (1/1, by vol.) electrolyte instead of PEO-based solid-state electrolyte in Li||NCM622 cells with Al foil current collector to investigate the decay of capacity. It can be found that adding 10 wt% LiTFSI in electrode material will also cause a reduction in discharge capacity (Fig. S4). However, localized corrosion of aluminum current collector was observed for liquid EC/DEC-LiTFSI electrolyte, whether or not 10 wt% fluor-lithium salt is added into the electrode material (Fig. S5a–c). This phenomenon also shows that in the solid-state electrolyte batteries, the corrosion behavior of aluminum foil current collector is much slower than that in the liquid batteries.

In light of high oxidation capability of the Ni⁴⁺/Ni³⁺ ions couple in Ni-rich cathode, the HOMO energy level of fluor-lithium salts and polyvinylidene fluoride (PVDF) are hence calculated under the same conditions (Fig. 1e). The HOMO reflects the difficulty of losing electrons in lithium salts [38], we can find that the HOMO for the investigated components decreases with the following order: PVDF < LiTFSI < LiFSI < LiDFOB, which is in the same order as the degree of capacity decay (13.7 mAh g⁻¹ < 20.1 mAh g⁻¹ < 29.1 mAh g⁻¹), indicating the LiTFSI, LiFSI, and LiDFOB are more prone to electron loss than PVDF, thus leading to oxidative decomposition. According their electrochemical windows (Fig. 1f), both LiTFSI and LiFSI exhibit cathodically stable

behavior up to 3.9 V (vs. Li/Li⁺), PVDF has a wide electrochemical stability window over 5.3 V, while LiDFOB is stable up to 4.75 V. However, the capacity of NCM622 cell with adding the LiDFOB into cathode materials is still significantly decayed, indicating that the high charging voltage of the NCM622 (4.3 V) cathode material is not a key factor to directly cause the decomposition of fluor-lithium salts, thus causing the capacity decay.

To address these problems mentioned above, XPS was employed to detect the surface of NCM622 cathode. Fig. 2a and b show the F 1s XPS spectra of NCM622 cathode with 10 wt% LiTFSI before and after cycling. The peaks at 687.8 eV and 688.9 eV can be assigned to the CF₂ of PVDF and CF₃ of LiTFSI, respectively [23,39–42]. The weak peak is observed at 684.8 eV for LiF without cycling, originating from part decomposition of LiTFSI during XPS measurements [37]. After three cycles, a new peak of 685.5 eV for NiF₂ appeared [42–44], indicating that the rapid decomposition of LiTFSI occurred during the charge/discharge process. The corresponding Ni 2p peaks appeared at 857.6 eV and 876.0 eV assigned to NiF₂ further demonstrate the corrosion reaction of LiTFSI with NCM622 (Fig. 2d and e) [18,45]. In contrast, the cycled NCM622 cathode without adding LiTFSI, no NiF₂ peak appears (Fig. 2c and f), while the intensity of peak (684.8 eV) for LiF increases. The results show that the PVDF does not cause surface corrosion of NCM622 cathode, and may involve the formation of CEI layer.

In consideration of the cells worked at 60 °C and high voltage of 4.3 V, a series of experiments have been conducted to investigate corrosion process. Firstly, NCM622 and LiTFSI were refluxed at 60 °C in tetrahydrofuran solution under nitrogen protection (Fig. 3a). After 24 h of treatment, the XRD patterns show no change compared to the initial NCM622 (Fig. 3b) [45–47], and no NiF₂ diffraction peak can be detectable for the treated NCM622 (Fig. 3c and d), which indicates the high temperature does not cause corrosion reaction between NCM622 and LiTFSI. Secondly, the Li||NCM622 cells with 10 wt% LiTFSI were carried out with various voltage ranges, such as 2.8–3.1 V, 2.8–3.7 V, and 2.8–4.3 V. As F 1s XPS spectra shown (Fig. 3e–g), the new peaks at 685.5 eV assigned to NiF₂ were observed in all voltage ranges. The

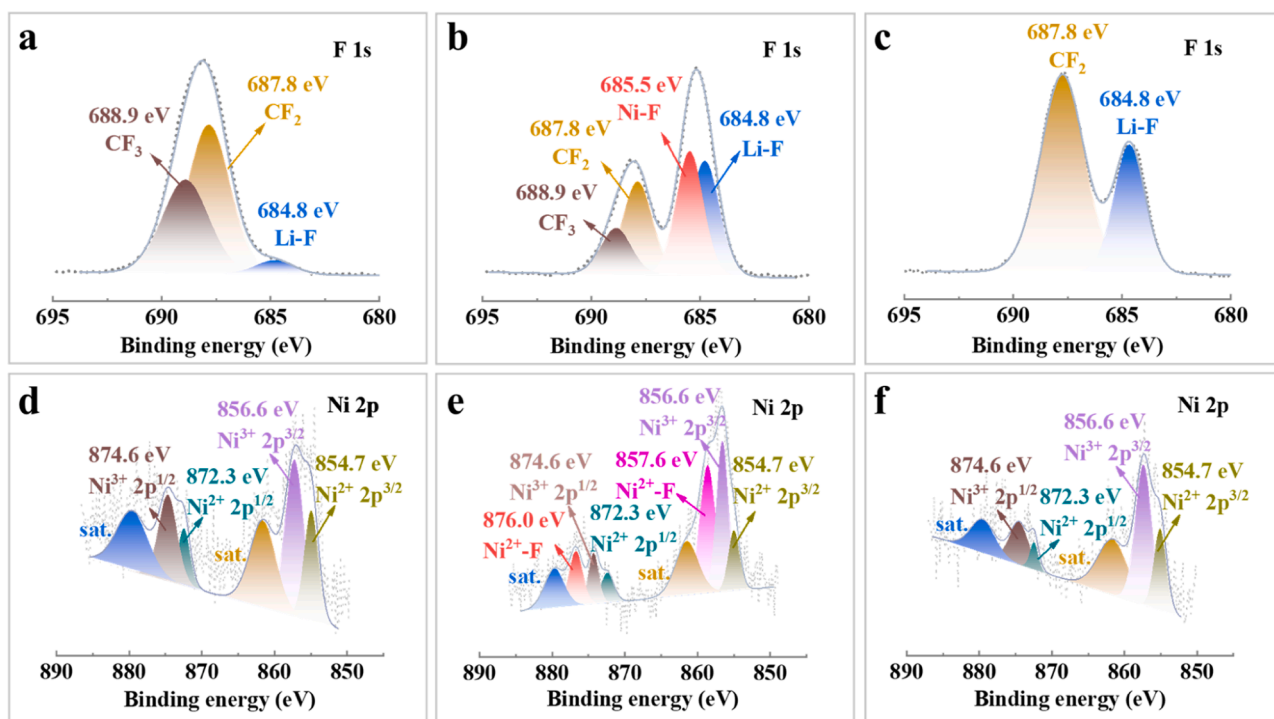


Fig. 2. (a) F 1s XPS spectrum of initial NCM622 with 10 wt% LiTFSI. (b) F 1s XPS spectrum of cycled NCM622 with 10 wt% LiTFSI. (c) F 1s XPS spectrum of cycled NCM622 without LiTFSI. (d) Ni 2p XPS spectrum of initial NCM622 with 10 wt% LiTFSI. (e) Ni 2p XPS spectrum of cycled NCM622 with 10 wt% LiTFSI. (f) Ni 2p XPS spectrum of cycled NCM622 without LiTFSI.

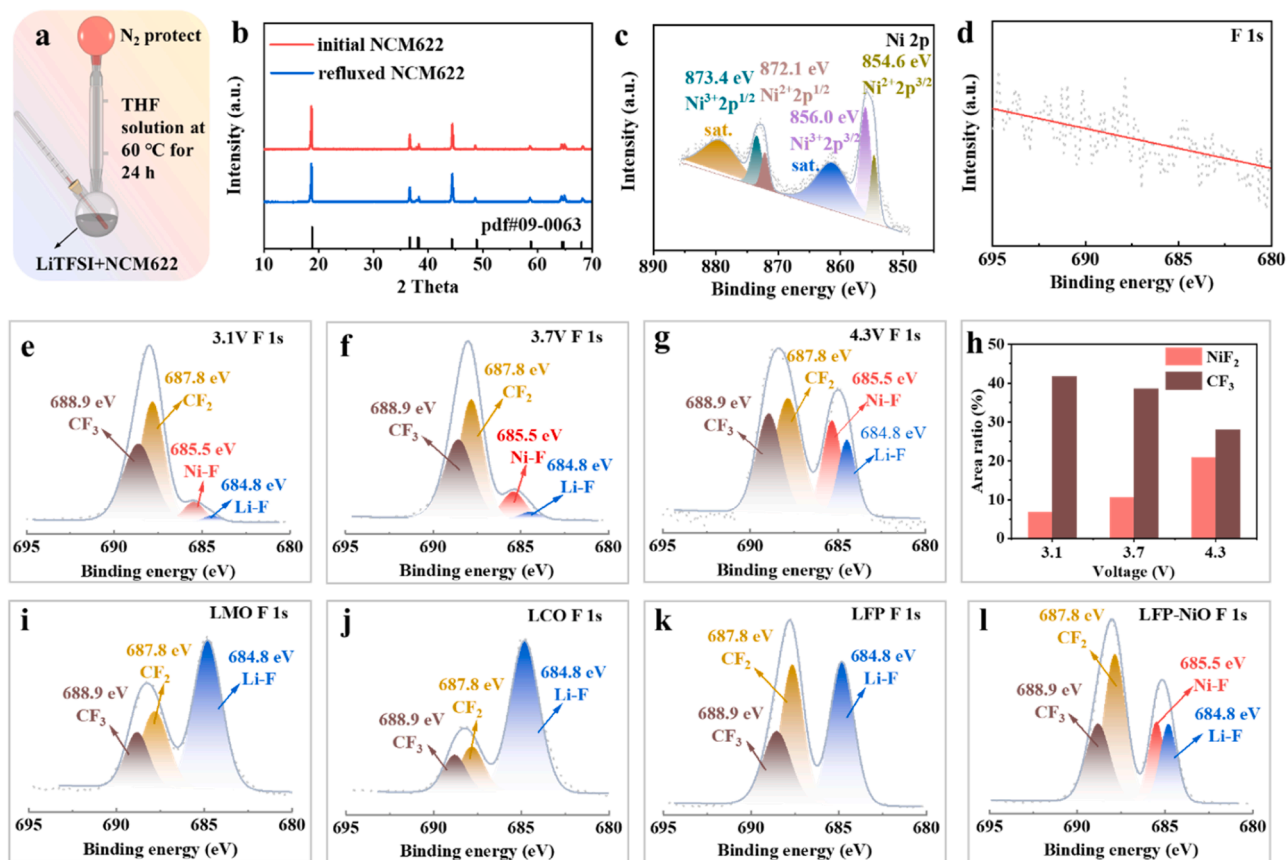


Fig. 3. (a) Schematic diagram of the device for LiTFSI and NCM622 reflux experiment. (b) XRD patterns of initial and refluxed NCM622. (c) Ni 2p XPS spectrum of refluxed NCM622. (d) F 1s XPS spectrum of refluxed NCM622. (e) F 1s spectrum of cycled NCM622 cathode with 10 wt% LiTFSI at cut-off voltage of 3.1 V. (f) F 1s spectrum of cycled NCM622 cathode with 10 wt% LiTFSI at cut-off voltage of 3.7 V. (g) F 1s spectrum of cycled NCM622 cathode with 10 wt% LiTFSI at cut-off voltage of 4.3 V. (h) Peak areas ratios of NiF₂ and CF₃ in the F 1s spectrum of NCM622 cathode with 10 wt% LiTFSI after cycling at different cut-off voltage. (i) F 1s XPS spectrum of cycled LMO cathode with 10 wt% LiTFSI. (j) F 1s XPS spectrum of cycled LCO cathode with 10 wt% LiTFSI. (k) F 1s XPS spectrum of cycled LFP cathode with 10 wt% LiTFSI. (l) F 1s XPS spectrum of cycled LFP cathode with 10 wt% LiTFSI and 10 wt% NiO.

intensity of NiF₂ peak on the surface of NCM622 cathode increases with increasing voltage intervals (Fig. 3h). These results indicate corrosion happened on the surface of the NCM622 in the presence of voltage, even at very low voltage interval of 2.8–3.1 V. However, a critical and confusing problem is whether the voltage is the only factor to stimulate corrosion. To combat this issue, under the same conditions, various cathode materials with 10 wt% LiTFSI, such as LiMn₂O₄ (LMO), LiCoO₂ (LCO), and LiFePO₄ (LFP) were assembled into Li||LMO (3.0–4.3 V), Li||LCO (3.0–4.3 V), and Li||LFP (2.5–4.2 V) cells, respectively. The charging and discharging curves are given in Figs. S6–S8, it can be found that all cells deliver stable initial discharge capacities compared with cells without LiTFSI, and almost no capacity loss occurs. The F 1s, Mn 2p, Co 2p, and Fe 2p XPS spectra further demonstrate that there is no metal fluoride produce (cobalt fluoride, manganese fluoride, and iron fluoride) (Figs. 3i–k and S9–S11). In contrast, both Li||NCM523 and Li||NCM811 cells with 10 wt% LiTFSI in cathode were also assembled under the same conditions, and subjected to charge and discharge cycling tests. Unsurprisingly, two cells displayed a significant capacity fading, about 16.7 mAh g⁻¹ for NCM523, and 16.1 mAh g⁻¹ for NCM811 (Figs. S12 and S13). Taken together with the observation of NCM622, the metal Ni²⁺ ions in Ni-rich cathode materials should be the core factor for capacity fading, and high voltage is the driving force to promote side reaction between NCM622 and LiTFSI (Figs. S14–S16). Finally, we also designed a contrast experiment that 10 wt% NiO was added into the LFP with 10 wt% LiTFSI cathode material, the discharge capacity retains stable (Fig. S17). However, after the initial three cycles at 60 °C and 0.1 C, XPS analysis results show that the surface of cathode contains NiF₂

salts (Figs. 3l and S18). These results indicate Ni²⁺ ions can as metal catalytic sites to induce the breakage of C-F bond in organic fluor-lithium salts, and promote the decomposition of organic fluor-lithium salts with the aid of voltage. While the formation of F⁻ anion will attack Ni-rich cathode surface to produce NiF₂, thus resulting in the corrosion behavior happened on surface of Ni-rich layered cathode materials. It is worth mentioning that other metal ions (Fe, Mn, and Co) are unable to arouse the same catalytic activity for C-F bond rupture, and the high ambient temperature of cells will accelerate corrosion reaction of Ni-rich cathode with LiTFSI (Fig. S19a–d).

To visualize the corrosion process, in situ XRD analysis of NCM811 cathodes without and with 10 wt% LiTFSI were performed during the charge/discharge processes. Fig. 4a and b show the diffraction pattern changed with increasing cycles during a scan from 2θ of 17.8° to 18.8°. The diffraction peak at 18.6° corresponds to (003) diffraction planes of NCM811, which is closely associated with the change of the lattice-parameter *c* [48–50]. It can be found that the diffraction peaks of NCM811 without LiTFSI maintain the same angle before and after the first cycle, but the diffraction peak of NCM811 with 10 wt% LiTFSI obviously shifts to the left side after first cycle, demonstrating that the local structural changes lead to the formation of surficial microcracks [51]. This can be attributed to corrosion occurred on the cathode surface, in which side reactions can corrode the electrode and cause structural degradation. As confirmed by the high-resolution SEM, we can clearly see that the surface of NCM811 particles with LiTFSI after cycling display high roughness and visible microcracks compared with the initial NCM811 and cycled without LiTFSI (Figs. 4c and d and S20).

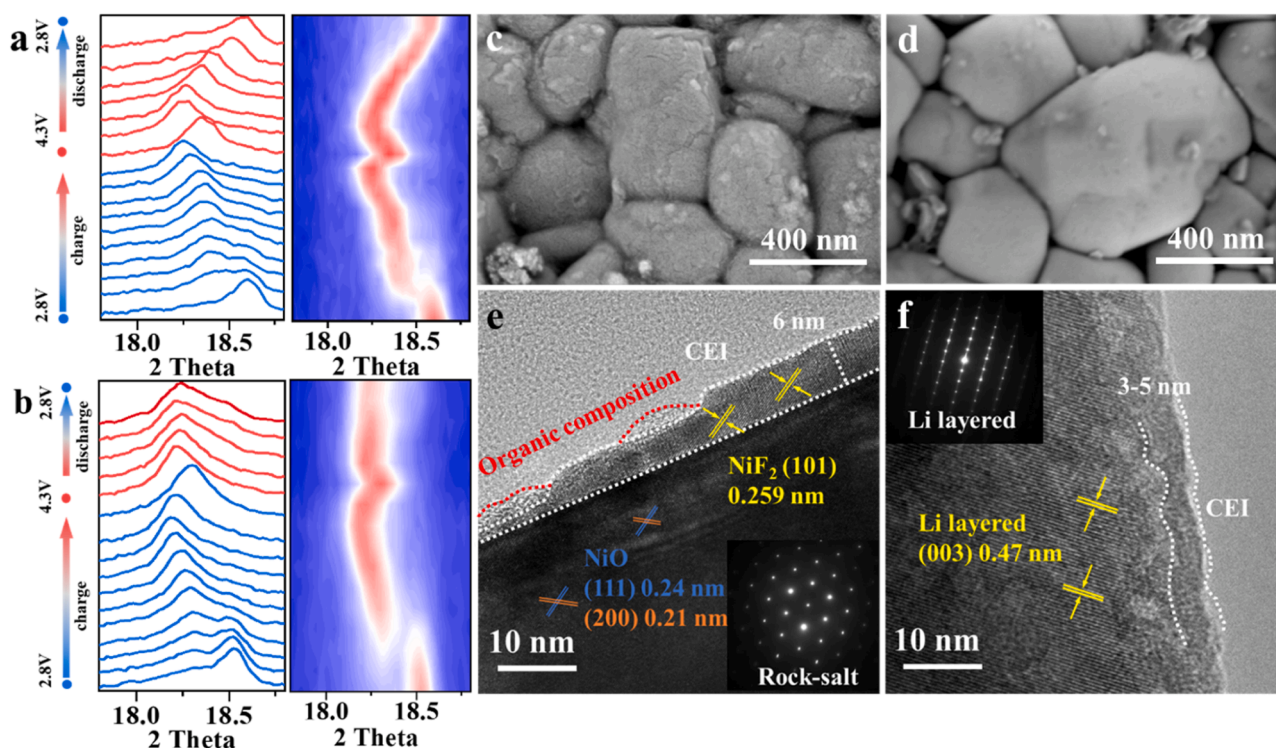


Fig. 4. (a) In situ XRD evolution of NCM811 without LiTFSI at the (003) diffraction peak during the first cycle. (b) In situ XRD evolution of NCM811 with 10wt% LiTFSI at the (003) diffraction peak during the first cycle. (c) SEM image of cycled NCM811 cathode with 10 wt% LiTFSI. (d) SEM image of cycled NCM811 cathode without LiTFSI. (e) TEM image of the cycled NCM811 cathode with 10 wt% LiTFSI, the inset shows the corresponding FFT patterns, (f) TEM image of the cycled NCM811 cathode without LiTFSI, the inset shows the corresponding FFT patterns.

As shown in Fig. S21, F element is evenly present on the surface of cycled NCM811 with 10 wt% LiTFSI, indicating that the NiF_2 is uniformly distributed on the cathode surface. Fig. 4e shows the TEM image of the cycled NCM811 cathode with LiTFSI, a SEI layer of around 6 nm was observed, which is mainly composed of inorganic-rich products (0.259 nm, NiF_2 (101)) derived from the corrosion reaction between cathode and TFSI^- anion [44], and a small amount of organic composition due to the decomposition of PEO-based electrolyte (Fig. 4e), under the same condition, the cycled NCM811 cathode without LiTFSI shows an about 3~5 nm CEI layer (Fig. 4f). The results indicate a large number of corrosion by-products on the cathode surface. In addition, it was found that two obvious lattice fringes have interlayer spacing of 0.21 nm and 0.24 nm on the surface of the cycled NCM811 cathode with LiTFSI, corresponding to the (111) and (200) crystal planes of NiO, respectively. Both are assigned to the rock-salt phase [52]. In contrast, the bulk phase of cycled NCM811 without LiTFSI still maintains a well-ordered layered structure (0.470 nm) (Fig. 4f) [53,54]. In addition, the corresponding fast Fourier transform (FFT) of bulk phase further confirms the presence of the rock-salt phase (Fig. 4e) [55,56]. These results indicate that partial nickel ions can be divorced from the Li-layered structure of NCM811, leading to the transformation of surficial layered structure to rock-salt phase.

In the light of the above experimental results, we propose the possible corrosion mechanism of the Ni-rich cathode through the four-process. As shown in Fig. 5a, the surface of NCM811 has abundant nickel vacancies in outer nickel layer, which provides the crucial sites for Ni^{2+} ions coordination with F atoms. The formation of Ni-F bond is beneficial to activate the adjacent C-F bond. As well reported in literatures [57–58], the strong C-F bond has high stability with an energy of 120~125 kcal mol⁻¹, which required high redox potential to mediate the C-F bond breakage. However, when the C-F bond to the nickel site, the C-F bond is weakened due to the nickel-catalyzed activation. Subsequently, under the driving force of external voltage, the C-F bond is

broken smoothly, and the Ni^{2+} ions also are detached from layered structure effected by the strong Ni-F bond. The corrosion process continue until the NiF_2 is completely formed on the surface of NCM811 cathode, as well as accompanied by a complete decomposition of LiTFSI.

To further determine voltage range that causes LiTFSI decomposition by nickel ions activation, the cyclic voltammetry (CV) was applied to the graphite||NCM811 cells with and without LiTFSI additive at the range of 0–2.8 V. Fig. S22 shows a strong oxidation peak in the cells without LiTFSI, which can be identified as the decomposition of the PEO-based electrolyte at the electrode-electrolyte interface. In contrast to the cells with LiTFSI additive, a clear reduction and oxidation peak appears around 1.35 V and 2.26 V during the first cycle, respectively, the former is assigned to the reduction of TFSI^- [23], the latter is attributed to the oxidative decomposition of TFSI^- on the NCM811 cathode surface. It is worth mentioning that the corresponding initial oxidative decomposition voltage occurs at 1.93 V (Fig. 5b), which is far smaller than the electrochemical window (3.9 V). Upon cycling, the oxidation peak at 2.26 V was weakened gradually and completely disappeared after three cycle. This phenomenon also reveals that the oxidative corrosion process primarily happened at the surface of NCM811 particles. After the continuous formation of passivation layer, it will further prevent the corrosion behavior, which is well consistent with the disappearance of oxidation peak (2.26 V). We conclude that the oxidative decomposition peak of LiTFSI should be over 1.93 V under the catalytic activation of nickel ions. The Tafel polarization curves of NCM811 cathode without and with 10 wt% LiTFSI are shown in Fig. 5c, the corrosion potential (E_{corr}) of NCM811 cathode with 10 wt% LiTFSI is 2.50 V, much lower than that of NCM811 cathode without LiTFSI ($E_{\text{corr}}=3.57$ V). The result shows that adding 10 wt% LiTFSI could obviously induce corrosion occurred on the surface of NCM811 cathode. It's worth noting that after three charge and discharge cycles, the E_{corr} of the NCM811 cathode with 10 wt% LiTFSI could return to 3.6 V, which is close to the E_{corr} of NCM811 cathode without LiTFSI (Fig. S23). The tendency demonstrates

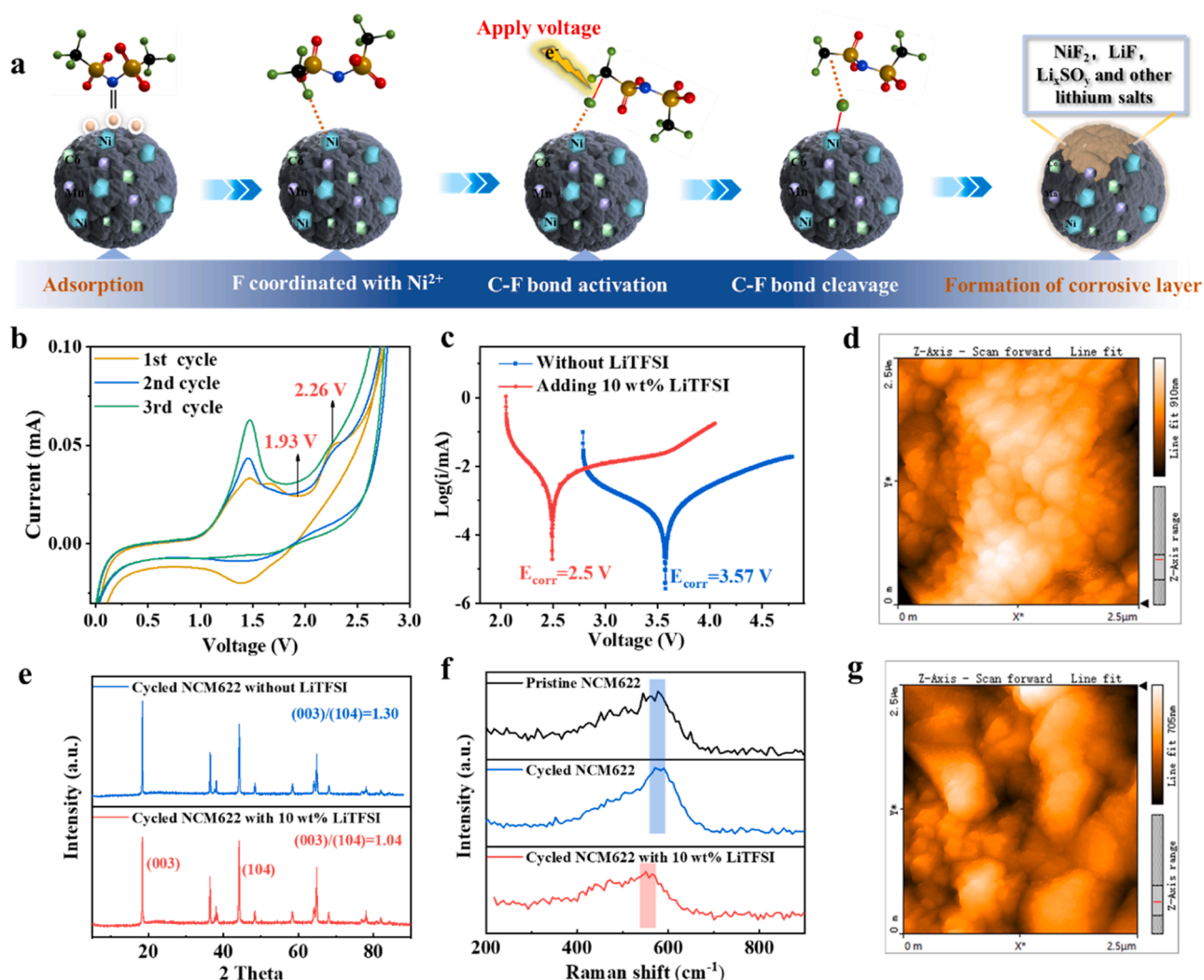


Fig. 5. (a) Schematic diagram of corrosion mechanism of Ni-rich cathode surface by LiTFSI. (b) CV curves of graphite||NCM811 cells with 10 wt% LiTFSI for 3 cycles. (c) The Tafel curves of Li||NCM811 cells with and without LiTFSI. (d) The AFM images of cycled NCM622 cathode without LiTFSI. (e) The ex situ XRD pattern of cycled NCM622 without and with 10 wt% LiTFSI. (f) The Raman spectrum of pristine NCM622, cycled NCM622 without LiTFSI, and cycled NCM622 with 10 wt% LiTFSI. (g) The AFM images of cycled NCM622 cathode with 10 wt% LiTFSI.

that the formed corrosion layer can inhibit further corrosion of the cathode. Fig. 5d and 5g present the atomic force microscope (AFM) pictures of cycled NCM622 cathode without and with 10 wt% LiTFSI. In contrast to the original and cycled NCM622 cathode (Figs. 5d and S24), the cycled NCM622 cathode with 10 wt% LiTFSI displays a fog-like corrosion layer on the surface of secondary particle and the secondary particle underwent deformation (Fig. 5g). As shown in Fig. 5e, the intensity ratio of (003)/(104) in cycled NCM622 without and with 10 wt% LiTFSI is 1.30 and 1.04, which indicates that the degree of $\text{Li}^+/\text{Ni}^{2+}$ mixed in the cycled NCM622 cathode with 10 wt% LiTFSI is higher than that of cycled NCM622 without LiTFSI, thus we concluded that introducing the LiTFSI can lead to more serious surface phase corrosion. This surface phase corrosion in the NCM622 cathode is further confirmed by Raman spectra (Fig. 5f), where the cycled NCM523 cathode with 10 wt% LiTFSI shows the left-shifted Raman peak due to the phase transformation of the layered phase into the rock-salt phase [59,60].

3. Conclusion

In a summary, we reveal the corrosion behavior of fluor-lithium salts toward the surface phase of Ni-rich cathode materials in all-solid-state lithium metal batteries. The addition of 10–30 wt% fluor-lithium salts

to the Ni-rich cathode materials results in discharge capacity loss in the first few cycles, which is not caused by Al collector corrosion but closely related to the surface phase corrosion of Ni-rich cathode materials by fluor-lithium salts. After investigation of corrosion mechanism, we found that the nickel ions of Ni-rich cathode can act as metal catalytic sites to induce the breakage of C-F bond of fluor-lithium salts driven by voltage. Other metal ions (iron, cobalt, and manganese) are unable to arouse the same catalytic activity for C-F bond rupture. Once corrosion occurs, the surface of NCM811 particles will produce a thick corrosion layer of around 6 nm, and corrosion process will also lead to the transformation of surficial layered structure to rock-salt phase. Our findings are of guidance for the rational preparation of high voltage Ni-rich cathode and the design of high-performance solid-state lithium metal batteries.

4. Experimental section

4.1. Preparation of composite cathode

The active materials (NCM622, NCM523, NCM811, LFP, LCO, LMO), Super P (SP), PVDF weighed in the ratio of 6:2:2 by mass and dissolve in N-Methylpyrrolidone (NMP), and the slurry was casted on the Al or Ti

current collector and dried in a vacuum oven at 80 °C for 12 h. The cathode foil was stamped into a small flat plate of 12 mm diameter and stored in a glove box with a loading of about 1.0 mg cm⁻² of active substance. As control groups, 10 wt%, 20 wt%, 30 wt% LiTFSI (mass fraction = $m_{\text{LiTFSI}}/m_{\text{Total}}$) were added to the slurry, and the above steps were repeated to obtain composite cathodes containing different mass fractions of LiTFSI. The cathode was prepared with the NCM811, SP, PVDF in the mass ratio of 90:5:5, and cycled to facilitate enrichment for TEM, SEM, XRD and Raman. The graphite|NCM811 full cells were used for cyclic voltammetry (CV) test, the cathode is made by uniformly mixing NCM811 and LiTFSI and pressing them into a plate. The anode consists of graphite, carboxymethyl cellulose, SP weighed in the ratio of 90:5:5, loading about 1.1 mg cm⁻².

4.2. Preparation of composite solid polymer electrolyte

Firstly, 50 mL of acetonitrile was used to dissolve the LiClO₄ (EO/Li=32/1 in molar ratio), SN, PEO, and dispersed the LLZTO. Then the mixture was stirred continuously at room temperature for 12 h to obtain a white uniform viscous liquid, which was then casted into a polytetrafluoroethylene mold and dried in a vacuum oven at 50 °C for 12 h. The final dried composite solid electrolyte film PEO-LiClO₄-LLZTO-SN was obtained, and the thickness of the electrolyte film was 60–80 μm.

4.3. Battery preparation and electrochemical testing

All electrochemical tests were carried out in R2025 type button cells. All cells were fabricated with lithium metal foil directly as anode in the glove box with argon atmosphere (H₂O<0.1 ppm, O₂<0.1 ppm) and all cells charging and discharging behaviors were performed under LAND CT2001A test system. Linear scanning voltammetry was performed on a VSP300 (Biologic) workstation at a scan rate of 5.0 mV s⁻¹ from 0 to 7.0 V. Li||SS cells were tested to evaluate the oxidation stability of each lithium salt as well as PVDF. The lithium salts and PVDF were dissolved in small amounts of acetonitrile and NMP, respectively, and a certain amount of the solution was pipetted onto the septum with a pipette gun, and the solvent was subsequently removed to obtain a containing only the lithium salts or PVDF as the electrolyte for Li||SS. This workstation was also used to record CV and Tafel curves.

4.4. Characterization

The X-ray photoelectron spectrometer (XPS, ASIS SUPRA) was used to analyze the material composition, elemental analysis and valence electron structure of the cathode surface during the experiment, all XPS spectra are calibrated using the C—C peak at binding energy of 284.6 eV as the reference. Scanning electron microscopy (SEM, Thermo Fisher Scientific Apreo S) and transmission electron microscopy (TEM, FEI Tecnai G2 F30, JEM ARM 200 F) were used to characterize the distribution and morphology of the cathode after cycling and the by-products on the cathode surface. For the EDS testing, to eliminate the influence of F element in fluor-lithium salt and PVDF on EDS mapping, the cycled cathodes were repeatedly cleaned using N, N-dimethylformamide and acetonitrile. X-ray diffraction (ex situ XRD, Bruker D8 Advance) was used to characterize the crystalline structure and phase composition of the cathode materials. In situ XRD (Bruker AXS D8 Advance) measurement was performed in an electrochemical cell with a beryllium window, and the active material slurry was casted on an Al foil. Atomic force microscopy (EasyScan 2, Nanosurf) was employed to measure the surface topography of NCM622 cathode with scanned area of 2.5 × 2.5 μm. Raman spectrometry (HORIBA Xplora Plus, excited by a 532 nm laser) offered insights into vibrational modes.

4.5. Theoretical calculations

The HOMO energy levels of PVDF, LiTFSI, LiFSI, and LiDFOB were

calculated using the Gaussian 09 package with 6-311+ g(d, p) as the basis group. In addition, PVDF calculates energy levels on a unit basis, all calculations are under the same condition.

CRedit authorship contribution statement

Hao Huang: Writing – original draft, Methodology, Investigation, Data curation. **Jingang Zheng:** Methodology, Investigation, Data curation, Conceptualization. **Hongyang Li:** Visualization, Software. **Siqi Guan:** Software, Methodology. **Hongwei Zhao:** Software, Methodology. **Weichen Han:** Methodology, Investigation. **Han Zhang:** Software, Data curation. **Guangshen Jiang:** Visualization, Data curation. **Lixiang Li:** Resources, Conceptualization. **Baigang An:** Writing – review & editing, Supervision, Funding acquisition. **Chengguo Sun:** Writing – review & editing, Supervision, Project administration, Funding acquisition.

Declaration of competing interest

The authors declare that they have no known competing financial interests or personal relationships that could have appeared to influence the work reported in this paper.

Acknowledgments

This work was supported by the National Natural Science Foundation of China (11972178, 52371224), the Natural Science Foundation of Liaoning Province (2023-BS-184), Technology Liaoning Project Grants (601010326), and Key Project supported by the Research Foundation of Education Bureau of Liaoning Province (no. JYTZD2023093).

Supplementary materials

Supplementary material associated with this article can be found, in the online version, at [doi:10.1016/j.ensm.2024.103953](https://doi.org/10.1016/j.ensm.2024.103953).

Data availability

Data will be made available on request.

References

- [1] T.T. Vu, H.J. Cheon, S.Y. Shin, G. Jeong, E. Wi, M. Chang, Hybrid electrolytes for solid-state lithium batteries: challenges, progress, and prospects, *Energy Storage Mater.* 61 (2023) 102876.
- [2] L. Nie, J.L. Zhu, X.Y. Wu, M.T. Zhang, X. Xiao, R.H. Gao, X.R. Wu, Y.F. Zhu, S. J. Chen, Z.Y. Han, Y. Yu, S.G. Wang, S.J. Ling, G.M. Zhou, A large-scale fabrication of flexible, ultrathin, and robust solid electrolyte for solid-state lithium-sulfur batteries, *Adv. Mater.* 36 (2024) 2400115.
- [3] S.Y. Ni, M.T. Zhang, C. Li, R.H. Gao, J.Z. Sheng, X. Wu, G.M. Zhou, 3D framework with Li₃N-Li₂S solid electrolyte interphase and fast ion transfer channels for stabilized lithium metal anode, *Adv. Mater.* 35 (2023) 2209028.
- [4] J.G. Zheng, C.G. Sun, Z.X. Wang, S.J. Liu, B.G. An, Z.H. Sun, F. Li, Double ionic–electronic transfer interface layers for all-solid-state lithium batteries, *Angew. Chem. Int. Edit.* 60 (2021) 18448–18453.
- [5] X.Wang Banerjee, C. Fang, E.A. Wu, Y.S. Meng, Interfaces and interphases in all-solid-state batteries with inorganic solid electrolytes, *Chem. Rev.* 120 (2020) 6878–6933.
- [6] R.Z. Tian, Z.Y. Wang, J.G. Liao, H.Z. Zhang, D.W. Song, L.Y. Zhu, L.Q. Zhang, High-voltage stability of small-size single crystal Ni-rich layered cathode for sulfide-based all-solid-state lithium battery at 4.5 V, *Adv. Energy Mater.* 13 (2023) 2300850.
- [7] W.B. Zhang, D.A. Weber, H. Weigand, T. Arlt, I. Manke, D. Schroder, R. Koerver, T. Leichtweiss, P. Hartmann, W.G. Zeier, J. Janek, Interfacial processes and influence of composite cathode microstructure controlling the performance of all-solid-state lithium batteries, *ACS Appl. Mater. Interface.* 9 (2017) 17835–17845.
- [8] S. Choi, M. Jeon, J. Ahn, W.D. Jung, S.M. Choi, J.S. Kim, J. Lim, Y.J. Jang, H. G. Jung, J.H. Lee, B.I. Sang, H. Kim, Quantitative analysis of microstructures and reaction interfaces on composite cathodes in all-solid-state batteries using a three-dimensional reconstruction technique, *ACS Appl. Mater. Interface.* 10 (2017) 23740–23747.

- [9] M.B. Dixit, A. Parejiya, N. Muralidharan, R. Essehli, R. Amin, I. Belharouak, Understanding implications of cathode architecture on energy density of solid-state batteries, *Energy Storage Mater.* 40 (2021) 239–249.
- [10] M. Ebner, D.W. Chung, R.E. Garcia, V. Wood, Tortuosity anisotropy in lithium-ion battery electrodes, *Adv. Energy Mater.* 4 (2014) 1301278.
- [11] Y.D. Kuang, C.J. Chen, D. Kirsch, L.B. Hu, Thick electrode batteries: principles, opportunities, and challenges, *Adv. Energy Mater.* 9 (2019) 1901457.
- [12] Bao, C. Zheng, M. Wu, Y. Zhang, J. Jin, H. Chen, Z. Wen, 12 μm -thick sintered garnet ceramic skeleton enabling high-energy-density solid-state lithium metal batteries, *Adv. Energy Mater.* 13 (2023) 2204028.
- [13] H. Duan, W.P. Chen, M. Fan, W.P. Wang, L. Yu, S.J. Tan, X. Chen, Q. Zhang, S. Xin, L.J. Wan, Y.G. Guo, Building an air stable and lithium deposition regulable garnet interface from moderate-temperature conversion chemistry, *Angew. Chem. Int. Edit.* 59 (2020) 12069–12075.
- [14] H.Y. Zhou, S.S. Yan, J. Li, H. Dong, P. Zhou, L. Wan, X.X. Chen, W.L. Zhang, Y. C. Xia, P.C. Wang, B.G. Wang, K. Liu, Lithium bromide-induced organic-rich cathode/electrolyte interphase for high-voltage and flame-retardant all-solid-state lithium batteries, *ACS Appl. Mater. Interface.* 14 (2022) 24469–24479.
- [15] M. Arrese-Igor, M. Martinez-Ibanez, E. Pavlenko, M. Forsyth, H.J. Zhu, M. Armand, F. Aguesse, P. Lopez-Aranguren, Toward high-voltage solid-state Li-metal batteries with double-layer polymer electrolytes, *ACS Energy Lett.* 7 (2022) 1473–1480.
- [16] M. Yao, Q. Ruan, T. Yu, H. Zhang, S. Zhang, Solid polymer electrolyte with in-situ generated fast Li^+ conducting network enable high voltage and dendrite-free lithium metal battery, *Energy Storage Mater.* 44 (2022) 93–103.
- [17] R. Fang, B. Xu, N.S. Grundish, Y. Xia, Y. Li, C. Lu, Y. Liu, N. Wu, J.B. Goodenough, Li_2S_6 -integrated PEO-based polymer electrolytes for all-solid-state lithium-metal batteries, *Angew. Chem. Int. Edit.* 60 (2021) 17701–17706.
- [18] M. Kim, B.D. Spindler, L. Dong, A. Stein, Li_2ZrO_6 as a pre-lithiation additive for lithium-ion batteries, *ACS Appl. Energy Mater.* 5 (2022) 14433–14444.
- [19] J.Y. Wang, R.S. Chen, L.F. Yang, M.W. Zan, P.H. Chen, Y. Li, W.J. Li, H.G. Yu, X. Q. Yu, X.J. Huang, L.Q. Chen, H. Li, Raising the intrinsic safety of layered oxide cathodes by surface re-lithiation with LLZTO garnet-type solid electrolytes, *Adv. Mater.* 34 (2022) 2200655.
- [20] Z. Zhang, S. Zhang, S. Geng, S. Zhou, Z. Hu, J. Luo, Agglomeration-free composite solid electrolyte and enhanced cathode-electrolyte interphase kinetics for all-solid-state lithium metal batteries, *Energy Storage Mater.* 51 (2022) 19–28.
- [21] K. Xu, Electrolytes and Interphases in Li-Ion Batteries and Beyond, *Chem. Rev.* 114 (2014) 11503–11618.
- [22] L.W. Dong, Y.P. Liu, D.J. Chen, Y.P. Han, Y.P. Ji, J.P. Liu, B.T. Yuan, Y.F. Dong, Q. Li, S.Y. Zhou, S.J. Zhong, Y.F. Liang, M.Q. Yang, C.H. Yang, W.D. He, Stabilization of high-voltage lithium metal batteries using a sulfone-based electrolyte with bi-electrode affinity and LiSO_2F -rich interphases, *Energy Storage Mater.* 44 (2022) 527–536.
- [23] Y. Liu, X. Tao, Y. Wang, C. Jiang, C. Ma, O. Sheng, G. Lu, X.W. Lou, Self-assembled monolayers direct a LiF-rich interphase toward long-life lithium metal batteries, *Science* 375 (2022) 739–745.
- [24] Sheng, J. Zheng, Z. Ju, C. Jin, Y. Wang, M. Chen, J. Nai, T. Liu, W. Zhang, Y. Liu, X. Tao, In situ construction of a LiF-enriched interface for stable all-solid-state batteries and its origin revealed by cryo-TEM, *Adv. Mater.* 32 (2020) 2000223.
- [25] E.J. Yoon, J.H. Lee, S.M. Byun, D.Y. Kim, T.H. Yoon, Passivation failure of Al current collector in LiPF_6 -based electrolytes for lithium-ion batteries, *Adv. Funct. Mater.* 32 (2022) 2200026.
- [26] Y. Luo, Y.J. Li, W.W. Sun, P.T. Xiao, S.K. Liu, D.Q. Wang, C.M. Zheng, Revisiting the corrosion mechanism of LiFSI based electrolytes in lithium metal batteries, *Electrochim. Acta* 419 (2022) 140353.
- [27] X. Huang, W.C. Zhu, J.Y. Yao, L.M. Bu, X.Y. Li, K. Tian, H. Lu, C.X. Quan, S.G. Xu, K.H. Xu, Z.K. Jiang, X. Zhang, L.J. Gao, J.Q. Zhao, Suppressing structural degradation of Ni-rich cathode materials towards improved cycling stability enabled by a Li_2MnO_3 coating, *J. Mater. Chem. A* 8 (2020) 17429–17441.
- [28] H. Maleki Kheimeh Sari, X. Li, Controllable cathode–electrolyte interface of $\text{Li}[\text{Ni}_{0.8}\text{Co}_{0.1}\text{Mn}_{0.1}]\text{O}_2$ for lithium ion batteries: a review, *Adv. Energy Mater.* 9 (2019) 1901597.
- [29] H.H. Sun, H.-H. Ryu, U.-H. Kim, J.A. Weeks, A. Heller, Y.-K. Sun, C.B. Mullins, Beyond doping and coating: prospective strategies for stable high-capacity layered Ni-rich cathodes, *ACS Energy Lett.* 5 (2020) 1136–1146.
- [30] X. Wang, X. Zhou, X.H. Liu, G.L. Feng, S. Wang, B. Zhang, P. Zhang, M.H. Zuo, W. Y. Xing, W.F. Wang, H. Zhang, G.P. Lv, W. Xiang, Surface reactivity versus microcracks in Ni-rich layered oxide cathodes: which is critical for long cycle life? *Chem. Eng. J.* 488 (2024) 150795.
- [31] S. Wang, X. Zhou, T. Zhao, J.L. Peng, B. Zhang, W.Y. Xing, M.H. Zuo, P. Zhang, W. F. Fan, G.P. Lv, W.B. Hua, W. Xiang, Precise regulation of particle orientation for Ni-rich cathodes with ultra-long cycle life, *Nano Energy* 129 (2024) 110008.
- [32] X. Zhou, F.F. Hong, S. Wang, T. Zhao, J.L. Peng, B. Zhang, W.F. Fan, W.Y. Xing, M. H. Zuo, P. Zhang, Y.H. Zhou, G.P. Lv, Y.J. Zhong, W.B. Hua, W. Xiang, Precision engineering of high-performance Ni-rich layered cathodes with radially aligned microstructure through architectural regulation of precursors, *eScience* (2024) 100276.
- [33] S.Q. Chen, P. Zhang, X. Zhou, W.B. Wu, X.H. Liu, Y.F. Liu, G.L. Feng, B. Zhang, W. Y. Xing, M.H. Zuo, P. Zhang, G.P. Lv, Y. Xiao, S.X. Dou, W. Xiang, Slightly Li-enriched chemistry enabling super stable $\text{LiNi}_{0.5}\text{Mn}_{0.5}\text{O}_2$ cathodes under extreme conditions, *Chem. Sci.* 15 (2024) 14415.
- [34] W.D. Li, A. Dolocan, P. Oh, H. Celio, S. Park, J. Cho, A. Manthiram, Heterogeneity in homogeneous nucleation from billion-atom molecular dynamics simulation of solidification of pure metal, *Nat. Commun.* 8 (2017) 10.
- [35] K.H. Nie, X.L. Wang, J.L. Qiu, Y. Wang, Q. Yang, J.J. Xu, X.Q. Yu, H. Li, X.J. Huang, L.Q. Chen, Increasing poly(ethylene oxide) stability to 4.5 V by surface coating of the cathode, *ACS Energy Lett.* 5 (2020) 826–832.
- [36] S.J. Xu, Z.H. Sun, C.G. Sun, F. Li, K. Chen, Z.H. Zhang, G.J. Hou, H.M. Cheng, F. Li, Homogeneous and fast ion conduction of PEO-based solid-state electrolyte at low temperature, *Adv. Funct. Mater.* 30 (2020) 2007172.
- [37] Z.J. Bi, S. Mu, N. Zhao, W.H. Sun, W.L. Huang, X.X. Guo, Cathode supported solid lithium batteries enabling high energy density and stable cyclability, *Energy Storage Mater.* 35 (2021) 512–519.
- [38] W.D. Zhang, S.Q. Zhang, L. Fan, L.N. Gao, X.Q. Kong, S.Y. Li, J. Li, X. Hong, Y. Y. Lu, Tuning the LUMO energy of an organic interphase to stabilize lithium metal batteries, *ACS Energy Lett.* 4 (2019) 644–650.
- [39] W. Yu, Z. Yu, Y. Cui, Z. Bao, Degradation and speciation of Li salts during XPS analysis for battery research, *ACS Energy Lett.* 7 (2022) 3270–3275.
- [40] Y. Liu, R. Hu, D. Zhang, J. Liu, F. Liu, J. Cui, Z. Lin, J. Wu, M. Zhu, Constructing Li-rich artificial SEI layer in alloy–polymer composite electrolyte to achieve high ionic conductivity for all-solid-state lithium metal batteries, *Adv. Mater.* 33 (2021) 2004711.
- [41] H. Yang, B. Zhang, M. Jing, X. Shen, L. Wang, H. Xu, X. Yan, X. He, In situ catalytic polymerization of a highly homogeneous PDOL composite electrolyte for long-cycle high-voltage solid-state lithium batterie, *Adv. Energy Mater.* 12 (2022) 2201762.
- [42] X. Fan, P. Chen, X. Yin, R.X. Qi, C. Yang, Y.J. Cheng, K. Guo, C. Liu, Y. Xia, One stone for multiple birds: a versatile cross-linked poly(dimethyl siloxane) binder boosts cycling life and rate capability of an NCM 523 cathode at 4.6 V, *ACS Appl. Mater. Interface.* 14 (2022) 16245–16257.
- [43] S. Hüfner, Analysis of the core level satellites in XPS spectra of Ni dihalides, *Solid State Commun* 49 (1984) 1177–1179.
- [44] Q. Chang, Z. Luo, L. Fu, J. Zhu, W. Yang, D. Li, L. Zhou, A new cathode material of NiF_2 for thermal batteries with high specific power, *Electrochim. Acta* 361 (2020) 137051.
- [45] Y.H. Luo, Q.L. Pan, H.X. Wei, Y.D. Huang, L.B. Tang, Z.Y. Wang, Z.J. He, C. Yan, J. Mao, K.H. Dai, X.H. Zhang, J.C. Zheng, Towards Ni-rich layered oxides cathodes with low Li/Ni intermixing by mild molten-salt ion exchange for lithium-ion batteries, *Nano Energy* 102 (2022) 107626.
- [46] H.H. Ryu, B. Namkoong, J.H. Kim, I. Belharouak, C.S. Yoon, Y.K. Sun, Capacity fading mechanisms in Ni-rich single-crystal NCM cathodes, *ACS Energy Lett.* 6 (2021) 2726–2734.
- [47] Y. Shi, G. Chen, F. Liu, X.J. Yue, Z. Chen, Resolving the compositional and structural defects of degraded $\text{LiNi}_x\text{Co}_y\text{Mn}_z\text{O}_2$ particles to directly regenerate high-performance lithium-ion battery cathodes, *ACS Energy Lett.* 3 (2018) 1683–1692.
- [48] H. Huang, Z.Q. Li, S. Gu, J.C. Bian, Y.Z. Li, J.J. Chen, K.M. Liao, Q.M. Gan, Y. F. Wang, S.S. Wu, Z.Y. Wang, W. Luo, R. Hao, Z.Q. Wang, G.Y. Wang, Z.G. Lu, Dextran sulfate lithium as versatile binder to stabilize high-voltage LiCoO_2 to 4.6 V, *Adv. Energy Mater.* 11 (2021) 2101864.
- [49] C.R. Zeng, F.X. Fan, R.X. Zheng, X.X. Wang, G.L. Tian, S. Liu, P.F. Liu, C. Wang, S. H. Wang, C.Z. Shu, Structure and charge regulation strategy enabling superior cycling stability of Ni-rich cathode materials, *ACS Appl. Mater. Interface.* 16 (2024) 11377–11388.
- [50] C.R. Zeng, R.X. Zheng, F.X. Fan, X.X. Wang, G.L. Tian, S. Liu, P.F. Liu, C. Wang, S. H. Wang, C.Z. Shu, Phase compatible surface engineering to boost the cycling stability of single-crystalline Ni-rich cathode for high energy density lithium-ion batteries, *Energy Storage Mater.* 72 (2024) 103788.
- [51] S.Q. Guan, L. Tao, P. Tang, R.P. Fang, H.Z. Wu, N. Piao, H.C. Yang, G.J. Hu, X. Geng, L.X. Li, B.G. An, F. Li, Regulating interfacial chemistry and kinetic behaviors of F/Mo co-doping Ni-rich layered oxide cathode for long-cycling lithium-ion batteries over -20°C – 60°C , *J. Energy Chem.* 94 (2024) 449–457.
- [52] W.Z. Yin, Z.G. Wu, W. Tian, Y.X. Chen, W. Xiang, G.L. Feng, Y.C. Li, C.J. Wu, C. L. Xu, C.J. Bai, B.H. Zhong, X.L. Wang, J. Zhang, F.R. He, A.A. Alshehri, X.D. Guo, Enhanced constraint and catalyzed conversion of lithium polysulfides via composite oxides from spent layered cathodes, *J. Mater. Chem. A* 7 (2019) 17867–17875.
- [53] T. Zhu, G.Q. Liu, D.L. Chen, J.X. Chen, P. Qi, J. Sun, X.Y. Gu, S. Zhang, Constructing flame-retardant gel polymer electrolytes via multiscale free radical annihilating agents for Ni-rich lithium batteries, *Energy Storage Mater.* 50 (2022) 495–504.
- [54] M. Chang, F.Y. Cheng, W. Zhang, J. Xu, Y. Zhang, T. Meng, S.X. Sun, Y. Xu, Q. Li, C. Fang, J.T. Han, Y.H. Huang, Antioxidant layer enables chemically stable cathode-electrolyte interface towards durable and safe Li-ion batteries, *Energy Storage Mater.* 61 (2023) 102872.
- [55] X. Cheng, Y. Li, T. Cao, R. Wu, M. Wang, H. Liu, X. Liu, J. Lu, Y. Zhang, Real-time observation of chemomechanical breakdown in a layered nickel-rich oxide cathode realized by in situ scanning electron microscopy, *ACS Energy Lett.* 6 (2021) 1703–1710.
- [56] N. Li, M. Sun, W.H. Kan, Z. Zhuo, S. Hwang, S.E. Renfrew, M. Avdeev, A. Huq, B. D. McCloskey, D. Su, W. Yang, W. Tong, Layered-rocksalt intergrown cathode for high-capacity zero-strain battery operation, *Nat. Commun.* 12 (2021) 2348.
- [57] X.L. Hu, Nickel-catalyzed cross coupling of non-activated alkyl halides: a mechanistic perspective, *Chem. Sci.* 2 (2021) 1867–1886.

- [58] H. Olivier-Bourbigou, P.A.R. Breuil, L. Magna, T. Michel, M.F.E. Pastor, D. Delcroix, Nickel catalyzed olefin oligomerization and dimerization, *Chem. Rev.* 120 (2020) 919–7983.
- [59] Y.H. Luo, Q.L. Pan, H.X. Wei, Y.D. Huang, L.B. Tang, Z.Y. Wang, C. Yan, J. Mao, K. H. Dai, Q. Wu, X.H. Zhang, J.C. Zheng, Regulating cation mixing for enhanced structural stability of layered oxide cathodes by ion-exchange strategy, *Mater. Today* 69 (2023) 54–65.
- [60] D. Eum, B. Kim, S.J. Kim, H. Park, J.P. Wu, S.P. Cho, G. Yoon, M.H. Lee, S.K. Jung, W.L. Yang, W.M. Seong, K. Ku, O. Tamwattana, S.K. Park, I. Hwang, K. Kang, Voltage decay and redox asymmetry mitigation by reversible cation migration in lithium-rich layered oxide electrodes, *Nat. Mater.* 19 (2020) 419–427.